

Search for an eV-scale sterile neutrino with the first six detection units of KM3NeT/ORCA

O. Adriani^{b,a} A. Albert^{c,be} A. R. Alhebsi^d S. Alshaloudi^d M. Alshamsi^e S. Alves Garre^f
 F. Ameli^g M. Andre^h L. Aphecetcheⁱ M. Ardid^j S. Ardid^j J. Aublin^k F. Badaracco^{m,l}
 L. Bailly-Salins¹ⁿ B. Baret^k A. Bariego-Quintana^f Y. Becherini^k M. Bendahman^o
 F. Benfenati Gualandi^{q,p} M. Benhassi^{r,o} D. M. Benoit^s Z. Beňušová^{u,t} E. Berbee^v
 E. Berti^b V. Bertin^e P. Betti^b S. Biagi^w M. Boettcher^x D. Bonanno^w M. Bondi^y
 S. Bottai^b A. B. Bouasla^{b,f} J. Boumaaza^z M. Bouda^e M. Bouwhuis^v C. Bozza^{aa,o}
 R. M. Bozza^{ab,o} H. Brâncăş^{ac} F. Breuhaus^e R. Bruijn^{ad,v} J. Brunner^e
 R. Bruno^y E. Buis^{v,ae} R. Buompane^{r,o} I. Burriel^f J. Buste^e B. Caiffi^m D. Calvo^f
 A. Capone^{g,af} F. Carenini^{q,p} V. Carretero^{ad,v} T. Cartraud^k P. Castaldi^{ag,p} V. Cecchini^f
 S. Celli^{g,af} L. Cerisy^e M. Chabab^{ah} A. Chen^{ai} S. Cherubini^{aj,w} T. Chiarusi^p
 W. Chung^{ak} M. Circella^{al} R. Clark^{am} R. Cocimano^w J. A. B. Coelho^k A. Coleiro^k A.
 Condorelli^k R. Coniglione^w P. Coyle^e A. Creusot^k G. Cuttone^w R. Dallierⁱ
 A. De Benedittis^{r,o} G. De Wasseige^{am} V. Decoeneⁱ P. Deguire^e I. Del Rosso^{q,p}
 L. S. Di Mauro^w I. Di Palma^{g,af} A. F. Díaz^{an} D. Diego-Tortosa^w C. Distefano^w
 A. Domi^{ao} C. Donzaud^k D. Dornic^e E. Drakopoulou^{ap} D. Drouhin^{c,be} J.-G. Ducoin^e
 P. Duverne^k R. Dvornický^u T. Eberl^{ao} E. Eckerová^{u,t} A. Eddymaoui^z T. van Eeden^v
 M. Eff^k D. van Eijk^v I. El Bojadaini^{aq} S. El Hedri^k S. El Mentawi^e V. Ellajosyula^m
 A. Enzenhöfer^e M. Farino^{ak} G. Ferrara^{aj,w} M. D. Filipović^{ar} F. Filippini^p
 D. Franciotti^w L. A. Fusco^{aa,o} T. Gal^{ao} J. García Méndez^j A. Garcia Soto^f
 C. Gatius Oliver^v N. Geißelbrecht^{ao} E. Genton^{am} H. Ghaddari^{aq} L. Gialanella^{r,o}
 B. K. Gibson^s E. Giorgio^w I. Goos^k P. Goswami^k S. R. Gozzini^f R. Gracia^{ao}
 B. Guillouⁿ C. Haack^{ao} C. Hanna^{ak} H. van Haren^{as} E. Hazelton^{ak} A. Heijboer^v
 L. Hennig^{ao} J. J. Hernández-Rey^f A. Idrissi^w W. Idrissi Ibnsalih^o G. Illuminati^p
 R. Jaimes^f O. Janik^{ao} D. Joly^e M. de Jong^{at,v} P. de Jong^{ad,v} B. J. Jung^v
 P. Kalaczyński^{bg,au} U. F. Katz^{ao} J. Keegans^s V. Kikvadze^{av} G. Kistauri^{aw,av}
 C. Kopper^{ao} A. Kouchner^{ax,k} Y. Y. Kovalev^{ay} L. Krupa^t V. Kueviakoe^v
 V. Kulikovskiy^m R. Kvataladze^{aw} M. Labalmeⁿ R. Lahmann^{ao} M. Lamoureux^{am}
 A. Langella^{ak} G. Larosa^w C. Lastoriaⁿ J. Lazar^{am} A. Lazo^f G. Lehautⁿ V. Lemaître^{am}
 E. Leonora^y N. Lessing^f G. Levi^{q,p} M. Lindsey Clark^k F. Longhitano^y S. Madarapu^f
 F. Magnani^e L. Malerba^{m,l} F. Mamedov^t A. Manfreda^o A. Manousakis^{az}
 M. Marconi^{l,m} A. Margiotta^{q,p} A. Marinelli^{ab,o} C. Markou^{ap} L. Martinⁱ
 M. Mastrodiicasa^{af,g} S. Mastroianni^o J. Mauro^{am} K. C. K. Mehta^{au} G. Miele^{ab,o}

¹Corresponding author

P. Migliozzi^o **E. Migneco^w** **M. L. Mitsou^{r,o}** **C. M. Mollo^o** **L. Morales-Gallegos^{r,o}**
N. Mori^b **A. Moussa^{aq}** **I. Mozun Mateoⁿ** **R. Muller^p** **M. R. Musone^{r,o}** **M. Musumeci^w**
S. Navas^{ba} **A. Nayerhoda^{al}** **C. A. Nicolau^g** **B. Nkosi^{ai}** **B. Ó Fearraigh^m** **V. Oliviero^{ab,o}**
A. Orlando^w **E. Oukacha^k** **L. Pacini^b** **D. Paesani^w** **J. Palacios González^f**
G. Papalashvili^{al,av} **P. Papini^b** **V. Parisi^{l,m}** **A. Parmarⁿ** **C. Pastore^{al}** **A. M. Păun^{ac}**
G. E. Păvălas^{ac} **S. Peña Martínez^k** **M. Perrin-Terrin^e** **V. Pestelⁿ** **M. Petropavlova^{t,bh}**
P. Piattelli^w **A. Plavin^{ay,bi}** **C. Poirè^{aa,o}** **V. Popa^{†2ac}** **T. Pradier^c** **J. Prado^f**
S. Pulvirenti^w **C.A. Quiroz-Rangel^j** **N. Randazzo^y** **A. Ratnani^{bb}** **S. Razzaque^{bc}**
I. C. Rea^o **D. Real^f** **G. Riccobene^w** **J. Robinson^x** **A. Romanov^{l,m,n}** **E. Ros^{ay}** **A. Šaina^f**
F. Salesa Greus^f **D. F. E. Samtleben^{at,v}** **A. Sánchez Losa^f** **S. Sanfilippo^w**
M. Sanguineti^{l,m} **D. Santonocito^w** **P. Sapienza^w** **M. Scaringella^b** **M. Scarnera^{am,k}**
J. Schnabel^{ao} **J. Schumann^{ao}** **J. Seneca^v** **P. A. Sevle Myhr^{am}** **I. Sgura^{al}** **R. Shanidze^{av}**
Chengyu Shao^{bj,e} **A. Sharma^k** **Y. Shitov^t** **F. Šimkovic^u** **A. Simonelli^o** **A. Sinopoulou^y**
B. Spisso^o **M. Spurio^{q,p}** **O. Starodubtsev^b** **D. Stavropoulos^{ap}** **I. Šteklt^t** **D. Stoccoⁱ**
M. Taiuti^{l,m} **Y. Tayalati^{z,bb}** **H. Thiersen^x** **S. Thoudam^d** **I. Tosta e Melo^{y,aj}** **B. Trocmé^k**
V. Tsourapis^{ap} **C. Tully^{ak}** **E. Tzamariudaki^{ap}** **A. Ukleja^{au}** **A. Vacheretⁿ** **V. Valsecchi^w**
V. Van Elewyck^{ax,k} **G. Vannoye^{l,m}** **E. Vannuccini^b** **G. Vasileiadis^{bd}** **F. Vazquez de Sola^v**
A. Veutro^{g,af} **S. Viola^w** **D. Vivolo^{r,o}** **A. van Vliet^d** **E. de Wolf^{ad,v}** **I. Lhenry-Yvon^k**
S. Zavatarelli^m **D. Zito^w** **J. D. Zornoza^f** **J. Zúñiga^f**

^aUniversità di Firenze, Dipartimento di Fisica e Astronomia, via Sansone 1, Sesto Fiorentino, 50019 Italy

^bINFN, Sezione di Firenze, via Sansone 1, Sesto Fiorentino, 50019 Italy

^cUniversité de Strasbourg, CNRS, IPHC UMR 7178, F-67000 Strasbourg, France

^dKhalifa University of Science and Technology, Department of Physics, PO Box 127788, Abu Dhabi, United Arab Emirates

^eAix Marseille Univ, CNRS/IN2P3, CPPM, Marseille, France

^fIFIC - Instituto de Física Corpuscular (CSIC - Universitat de València), c/Catedrático José Beltrán, 2, 46980 Paterna, Valencia, Spain

^gINFN, Sezione di Roma, Piazzale Aldo Moro, 2 - c/o Dipartimento di Fisica, Edificio, G.Marconi, Roma, 00185 Italy

^hUniversitat Politècnica de Catalunya, Laboratori d'Aplicacions Bioacústiques, Centre Tecnològic de Vilanova i la Geltrú, Avda. Rambla Exposició, s/n, Vilanova i la Geltrú, 08800 Spain

ⁱSubatech, IMT Atlantique, IN2P3-CNRS, Nantes Université, 4 rue Alfred Kastler - La Chantrerie, Nantes, BP 20722 44307 France

^jUniversitat Politècnica de València, Instituto de Investigación para la Gestión Integrada de las Zonas Costeras, C/ Paranimf, 1, Gandia, 46730 Spain

^kUniversité Paris Cité, CNRS, Astroparticule et Cosmologie, F-75013 Paris, France

^lUniversità di Genova, Via Dodecaneso 33, Genova, 16146 Italy

^mINFN, Sezione di Genova, Via Dodecaneso 33, Genova, 16146 Italy

ⁿLPC CAEN, Normandie Univ, ENSICAEN, UNICAEN, CNRS/IN2P3, 6 boulevard Maréchal Juin, Caen, 14050 France

^oINFN, Sezione di Napoli, Complesso Universitario di Monte S. Angelo, Via Cintia ed. G, Napoli, 80126 Italy

²Deceased

^p*INFN, Sezione di Bologna, v.le C. Berti-Pichat, 6/2, Bologna, 40127 Italy*

^q*Università di Bologna, Dipartimento di Fisica e Astronomia, v.le C. Berti-Pichat, 6/2, Bologna, 40127 Italy*

^r*Università degli Studi della Campania "Luigi Vanvitelli", Dipartimento di Matematica e Fisica, viale Lincoln 5, Caserta, 81100 Italy*

^s*E. A. Milne Centre for Astrophysics, University of Hull, Hull, HU6 7RX, United Kingdom*

^t*Czech Technical University in Prague, Institute of Experimental and Applied Physics, Husova 240/5, Prague, 110 00 Czech Republic*

^u*Comenius University in Bratislava, Department of Nuclear Physics and Biophysics, Mlynska dolina F1, Bratislava, 842 48 Slovak Republic*

^v*Nikhef, National Institute for Subatomic Physics, PO Box 41882, Amsterdam, 1009 DB Netherlands*

^w*INFN, Laboratori Nazionali del Sud, (LNS) Via S. Sofia 62, Catania, 95123 Italy*

^x*North-West University, Centre for Space Research, Private Bag X6001, Potchefstroom, 2520 South Africa*

^y*INFN, Sezione di Catania, (INFN-CT) Via Santa Sofia 64, Catania, 95123 Italy*

^z*University Mohammed V in Rabat, Faculty of Sciences, 4 av. Ibn Battouta, B.P. 1014, R.P. 10000 Rabat, Morocco*

^{aa}*Università di Salerno e INFN Gruppo Collegato di Salerno, Dipartimento di Fisica, Via Giovanni Paolo II 132, Fisciano, 84084 Italy*

^{ab}*Università di Napoli "Federico II", Dip. Scienze Fisiche "E. Pancini", Complesso Universitario di Monte S. Angelo, Via Cintia ed. G, Napoli, 80126 Italy*

^{ac}*Institute of Space Science - INFNPR Subsidiary, 409 Atomistilor Street, Magurele, Ilfov, 077125 Romania*

^{ad}*University of Amsterdam, Institute of Physics/IHEF, PO Box 94216, Amsterdam, 1090 GE Netherlands*

^{ae}*TNO, Technical Sciences, PO Box 155, Delft, 2600 AD Netherlands*

^{af}*Università La Sapienza, Dipartimento di Fisica, Piazzale Aldo Moro 2, Roma, 00185 Italy*

^{ag}*Università di Bologna, Dipartimento di Ingegneria dell'Energia Elettrica e dell'Informazione "Guglielmo Marconi", Via dell'Università 50, Cesena, 47521 Italia*

^{ah}*Cadi Ayyad University, Physics Department, Faculty of Science Semlalia, Av. My Abdellah, P.O.B. 2390, Marrakech, 40000 Morocco*

^{ai}*University of the Witwatersrand, School of Physics, Private Bag 3, Johannesburg, Wits 2050 South Africa*

^{aj}*Università di Catania, Dipartimento di Fisica e Astronomia "Ettore Majorana", (INFN-CT) Via Santa Sofia 64, Catania, 95123 Italy*

^{ak}*Princeton University, Department of Physics, Jadwin Hall, Princeton, New Jersey, 08544 USA*

^{al}*INFN, Sezione di Bari, via Orabona, 4, Bari, 70125 Italy*

^{am}*UCLouvain, Centre for Cosmology, Particle Physics and Phenomenology, Chemin du Cyclotron, 2, Louvain-la-Neuve, 1348 Belgium*

^{an}*University of Granada, Department of Computer Engineering, Automation and Robotics / CITIC, 18071 Granada, Spain*

^{ao}*Friedrich-Alexander-Universität Erlangen-Nürnberg (FAU), Erlangen Centre for Astroparticle Physics, Nikolaus-Fiebiger-Straße 2, 91058 Erlangen, Germany*

^{ap}*NCSR Demokritos, Institute of Nuclear and Particle Physics, Ag. Paraskevi Attikis, Athens, 15310 Greece*

^{aq} University Mohammed I, Faculty of Sciences, BV Mohammed VI, B.P. 717, R.P. 60000 Oujda, Morocco

^{ar} Western Sydney University, School of Science, Locked Bag 1797, Penrith, NSW 2751 Australia

^{as} NIOZ (Royal Netherlands Institute for Sea Research), PO Box 59, Den Burg, Texel, 1790 AB, the Netherlands

^{at} Leiden University, Leiden Institute of Physics, PO Box 9504, Leiden, 2300 RA Netherlands

^{au} AGH University of Krakow, Al. Mickiewicza 30, 30-059 Krakow, Poland

^{av} Tbilisi State University, Department of Physics, 3, Chavchavadze Ave., Tbilisi, 0179 Georgia

^{aw} The University of Georgia, Institute of Physics, Kostava str. 77, Tbilisi, 0171 Georgia

^{ax} Institut Universitaire de France, 1 rue Descartes, Paris, 75005 France

^{ay} Max-Planck-Institut für Radioastronomie, Auf dem Hügel 69, 53121 Bonn, Germany

^{az} University of Sharjah, Sharjah Academy for Astronomy, Space Sciences, and Technology, University Campus - POB 27272, Sharjah, - United Arab Emirates

^{ba} University of Granada, Dpto. de Física Teórica y del Cosmos & C.A.F.P.E., 18071 Granada, Spain

^{bb} School of Applied and Engineering Physics, Mohammed VI Polytechnic University, Ben Guerir, 43150, Morocco

^{bc} University of Johannesburg, Department Physics, PO Box 524, Auckland Park, 2006 South Africa

^{bd} Laboratoire Univers et Particules de Montpellier, Place Eugène Bataillon - CC 72, Montpellier Cédex 05, 34095 France

^{be} Université de Haute Alsace, rue des Frères Lumière, 68093 Mulhouse Cedex, France

^{bf} Université Badji Mokhtar, Département de Physique, Faculté des Sciences, Laboratoire de Physique des Rayonnements, B. P. 12, Annaba, 23000 Algeria

^{bg} AstroCeNT, Nicolaus Copernicus Astronomical Center, Polish Academy of Sciences, Rektorska 4, Warsaw, 00-614 Poland

^{bh} Charles University, Faculty of Mathematics and Physics, Ovocný trh 5, Prague, 116 36 Czech Republic

^{bi} Harvard University, Black Hole Initiative, 20 Garden Street, Cambridge, MA 02138 USA

^{bj} School of Physics and Astronomy, Sun Yat-sen University, Zhuhai, China

E-mail: baillysalins@lpsc.in2p3.fr, km3net-pc@km3net.de

ABSTRACT: The existence of an eV-scale sterile neutrino has been proposed to explain several anomalous experimental results obtained over the course of the past 25 years. The first search for such a sterile neutrino conducted with data from KM3NeT/ORCA — a water Cherenkov neutrino telescope under construction at the bottom of the Mediterranean Sea — is reported in this paper. GeV-scale atmospheric neutrino oscillations are measured by reconstructing the energy and arrival direction of up-going neutrinos that have traversed the Earth. This study is based on a data sample containing 5828 neutrino candidates collected with 6 detection units (5% of the complete detector), corresponding to an exposure of 433 kton-years. From the expected effect of an eV-scale sterile neutrino on the first $\nu_\mu \rightarrow \nu_\tau$ standard oscillation maximum, simultaneous constraints are put on the magnitude of the $U_{\mu 4}$ and $U_{\tau 4}$ mixing elements assuming $\Delta m_{41}^2 \geq 1 \text{ eV}^2$. The results are compatible with the absence of mixing between active neutrinos and a sterile state, with $|U_{\mu 4}|^2 < 0.138$ and $|U_{\tau 4}|^2 < 0.076$ at a 90% confidence level. Such constraints are compatible with the results reported by other long-baseline experiments, and indicate that with KM3NeT/ORCA it is possible to bring crucial contributions to sterile neutrino searches in the coming years.

Contents

1	Introduction	1
2	Effect of an eV-scale sterile neutrino on the oscillation probabilities	2
3	The KM3NeT/ORCA detector	5
4	ORCA6 data sample and event selection	8
5	Analysis method	9
5.1	Event distribution modeling and Monte Carlo simulations	9
5.2	Nuisance parameters	9
5.3	Statistical methods	10
5.4	Fitting procedure	11
6	Results	12
6.1	Best-fit point	12
6.2	$(U_{\mu 4} ^2, U_{\tau 4} ^2)$ scan results	13
6.3	Comparison with existing measurements	14
7	Conclusion	16

1 Introduction

Since their first observation in 1998 [1, 2], neutrino oscillations have been modeled through the three-flavour Pontecorvo-Maki-Nakagawa-Sakata (PMNS) paradigm [3]. The model describes the mixing between the neutrino flavour eigenstates (ν_e, ν_μ, ν_τ) and the neutrino mass eigenstates (ν_1, ν_2, ν_3) of masses (m_1, m_2, m_3). In this formalism, the PMNS matrix is a 3-by-3 rotation matrix parametrised by the three mixing angles θ_{12}, θ_{13} and θ_{23} and the Dirac CP-violating phase δ . The mixing angles determine the extent of mixing between the neutrino states, while the CP-violating phase breaks the symmetry of oscillation probabilities for neutrinos and antineutrinos. The frequencies of the observed oscillations are determined by the values of two independent squared-mass differences, for example Δm_{31}^2 and Δm_{21}^2 . Over the past 25 years, experiments using various neutrino sources have significantly improved the precision in measuring these six oscillation parameters, with uncertainties currently down to the percent level [4]. However, the δ phase is still largely unconstrained by experiments. The θ_{23} octant (whether it is lower than, equal to or higher than $\pi/4$) is also undetermined. Finally, the sign of Δm_{31}^2 , determining the neutrino mass ordering (NMO) which is either normal ($m_1 < m_2 < m_3$, NO) or inverted ($m_3 < m_1 < m_2$, IO), is also unknown. Current and upcoming large-scale neutrino oscillation experiments

will pursue these questions over the next decade to deepen our understanding of neutrino properties.

Despite the success of the three-flavour PMNS paradigm at describing the neutrino oscillation data, several experimental results obtained at a relatively short baseline (SBL) remain largely unexplained [5]. All these anomalies, despite originating from experiments with different neutrino sources, detection technologies, oscillation channels, baselines and neutrino energies, can be individually interpreted as oscillations driven by a squared-mass difference $\Delta m^2 \sim \mathcal{O}(1)$ eV². This value of Δm^2 is several orders of magnitude larger than the measured values of Δm_{31}^2 and Δm_{21}^2 . Thus, to explain the SBL anomalies in terms of oscillations, a simple extension of the standard model is to assume the existence of a fourth, eV-scale, neutrino state. However, cosmological constraints exist on the effective number of relativistic neutrino species [6, 7]. In addition, the LEP experiments obtained compelling evidence that only three flavours of light neutrinos that couple to the weak interaction — known as active neutrinos — exist [8].¹ Thus, an additional eV-scale neutrino would have to be insensitive to the weak interaction, or sterile. In the following, this model will be referred to as the 3+1 model.

The presence of an eV-scale sterile neutrino would also alter the oscillation probabilities of neutrinos detected in experiments with longer baselines such as atmospheric neutrino telescopes. The IceCube collaboration recently reported updated results of searches for an eV-scale sterile neutrino using their complete detector [9, 10] as well as using the denser DeepCore array [11]. In the present work, the first search for an eV-scale sterile neutrino performed with data from the KM3NeT/ORCA detector is presented. After a review of the effect of an eV-scale sterile neutrino on the oscillation channels of interest in section 2, the KM3NeT/ORCA water Cherenkov neutrino telescope is presented in section 3. The dataset used in this study was collected with an early partial configuration of the detector with six detection units, called ORCA6 in the following, operating from January 2020 to November 2021. The data sample as well as the event selection strategy is presented in section 4. The model and statistical methods used to perform this oscillation analysis are presented in section 5. Finally, the results are summarised and discussed in sections 6 and 7 respectively.

2 Effect of an eV-scale sterile neutrino on the oscillation probabilities

Oscillations in the presence of a single sterile neutrino can be modeled by extending the standard three-flavour formalism to include a fourth mass eigenstate m_4 . This extension introduces one additional squared-mass difference, usually denoted by Δm_{41}^2 . The PMNS matrix becomes a 4×4 unitary matrix $U_{\alpha i}$ with $\alpha = e, \mu, \tau, s$ and $i = 1, 2, 3, 4$, which can be parametrised such that:

$$U = R_{34} \tilde{R}_{24} \tilde{R}_{14} R_{23} \tilde{R}_{13} R_{12}, \quad (2.1)$$

¹In that context, light means with a mass lower than half of the mass of the Z boson.

where R_{jk} is a rotation matrix in the j - k plane and, similarly, \tilde{R}_{jk} is a unitary rotation matrix with an added complex phase. In addition to the three standard mixing angles and the Dirac CP violation phase, three active-sterile mixing angles θ_{i4} , $i = 1, 2, 3$, and two additional Dirac CP violation phases δ_{i4} , $i = 1, 2$ are usually introduced to parametrise the extended matrix. The active-sterile mixing angles are related to the active-sterile mixing elements by:

$$U_{e4} = \sin \theta_{14} e^{-i\delta_{14}} \quad (2.2)$$

$$U_{\mu 4} = \cos \theta_{14} \sin \theta_{24} e^{-i\delta_{24}} \quad (2.3)$$

$$U_{\tau 4} = \cos \theta_{14} \cos \theta_{24} \sin \theta_{34}. \quad (2.4)$$

In addition to the intrinsic vacuum effect of the added mass eigenstate on the oscillation probabilities, matter effects are critically important in the 3+1 model. When active neutrinos propagate through a medium, they experience the weak potential induced by the nucleons and electrons within the matter. This leads to coherent forward scattering [12], which can occur for all active flavours via neutral current (NC) interactions with neutrons, protons and electrons, and for ν_e or $\bar{\nu}_e$ via charged current (CC) interactions with electrons. For the CC channel, the corresponding effective potential is [13]:

$$V_{\text{CC}} = \pm \sqrt{2} G_F N_e, \quad (2.5)$$

where G_F is the Fermi constant, N_e the electron density of the medium and V_{CC} is positive for ν_e , negative for $\bar{\nu}_e$. Neutral current interactions with neutrons, protons and electrons are equally possible for ν_e , ν_μ and ν_τ . The corresponding potential is:

$$V_{\text{NC}} = V_{\text{NC}}^n + V_{\text{NC}}^p + V_{\text{NC}}^{e^-} \quad (2.6)$$

where, due to equal densities of protons and electrons in ordinary matter and to their opposite charge, the potentials V_{NC}^p and $V_{\text{NC}}^{e^-}$ cancel out. Only the neutron-induced potential remains, yielding:

$$V_{\text{NC}} = \mp \frac{1}{2} \sqrt{2} G_F N_n \quad (2.7)$$

where N_n is the neutron density of the medium and V_{NC} is negative for ν , positive for $\bar{\nu}$.

In the standard three-flavour case, matter effects arise as only electron (anti)neutrinos are affected by V_{CC} , impacting their propagation and altering the oscillation patterns with respect to the vacuum case. However, all three flavours experience the same NC potential from neutrons, so no flavour-dependent coherent forward scattering is introduced by V_{NC} . Conversely, in the 3+1 case, sterile neutrinos are not affected by V_{NC} , with the neutrino propagation being described by the following Hamiltonian in the flavour basis:

$$H_{\text{fl}} = U H_0 U^\dagger + V_{4\nu} \quad (2.8)$$

where U is the 3+1 PMNS matrix in vacuum, $H_0 = \frac{1}{2E} \text{diag}(0, \Delta m_{21}^2, \Delta m_{31}^2, \Delta m_{41}^2)$ is the Hamiltonian in vacuum in the mass basis and $V_{4\nu} = \text{diag}(V_{\text{CC}}, 0, 0, -V_{\text{NC}})$, where V_{NC} has been subtracted from the diagonal.

When accounting for matter effects in the 3+1 case, the oscillation probabilities become very complex and difficult to express analytically. Some approximations can be made for specific regimes of Δm_{41}^2 and neutrino energy, as shown in [14]. Preliminary studies [15] showed that ORCA6 has no sensitivity to the θ_{14} mixing angle, as it mainly affects the ν_e disappearance channel, where the detector's sensitivity is limited. Thus, $\theta_{14} = 0$ (and consequently $\delta_{14} = 0$) is considered in the following. An analytical formula for $P(\nu_\mu \rightarrow \nu_\mu)$ (not used in this work) has been derived under the assumption $\theta_{14} = \theta_{13} = \theta_{12} = 0$ in [16] and extended in the appendix of [17] to include the effect of δ_{24} . The preliminary studies in [18] also showed that ORCA6 has poor sensitivity to very light sterile neutrinos with $\Delta m_{41}^2 < 10^{-2}$ eV² and that its sensitivity to both θ_{24} and θ_{34} is mostly independent of $\Delta m_{41}^2 > 10^{-1}$ eV², as the fast oscillations induced by increasing values of Δm_{41}^2 are smeared out due to detector effects. Thus, for simplicity, $\Delta m_{41}^2 = 1$ eV² is considered in the following, and the results are assumed to be valid for $\Delta m_{41}^2 \geq 1$ eV². The difference in ν_μ survival probability between the three-flavour case and the 3+1 case with $\Delta m_{41}^2 = 1$ eV² and $\sin^2 \theta_{24} = 0.1$ (all other sterile parameters being set to 0) is shown in figure 1, where normal ordering is assumed. The probabilities are shown for atmospheric neutrinos (left) and antineutrinos (right) crossing the Earth, as a function of the neutrino energy E_ν and the cosine of its zenith angle θ . The zenith angle is defined as the angle between the neutrino direction and the upwards vertical at the detector position, and is directly related to the neutrino propagation length inside the Earth, L .² The effects of the fast $\nu_\mu \rightarrow \nu_s$ oscillations can be seen in both cases, lowering the ν_μ survival probability on average in the whole energy and $\cos \theta$ range. Two striking features appear in the eV sterile case: on the left, the reduced ν_μ disappearance at around 25 GeV for vertical neutrinos; and on the right, the enhanced $\bar{\nu}_\mu$ disappearance at TeV energies. Although they happen at very different energies, both are matter-induced effects.

The TeV $\bar{\nu}_\mu$ disappearance resonance was established more than twenty years ago as a distinctive signature of an eV-scale sterile neutrino in atmospheric neutrino oscillations [21]. As seen in figure 1, the effect is more prominent at $E_\nu \simeq 5$ TeV for mantle-only crossing trajectories ($\cos \theta > -0.838$). It can be interpreted as the consequence of the Mikheyev-Smirnov-Wolfenstein effect [12, 22, 23] in the Earth's mantle. The $\bar{\nu}_\mu$ disappearance peak corresponds to a conversion into an almost pure sterile state [15]. This feature has been extensively used in analyses of IceCube data to constrain the θ_{24} mixing angle as a function of Δm_{41}^2 [9, 24–27]. For KM3NeT/ORCA, the statistics of TeV-scale neutrinos are limited because of its comparatively smaller detector size.

Instead, the analysis presented in this paper primarily focuses on the lower energy feature highlighted in figure 1 (left). While the average effect of the presence of the sterile neutrino is an overall decrease of the ν_μ survival probability compared to the three-flavour case, there is a notable exception. For the most vertical neutrinos, crossing both the mantle and the core ($\cos \theta < -0.838$), there is a region around 25 GeV where less muon neutrinos

² $\cos \theta = -1$ corresponds to vertical up-going neutrinos and $\cos \theta = 0$ to horizontal neutrinos.

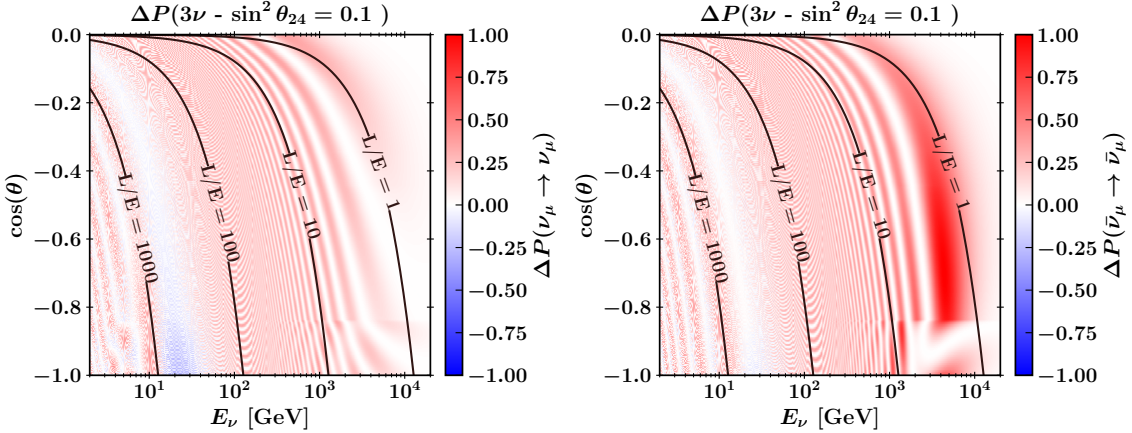


Figure 1. Difference in muon neutrino (left) and antineutrino (right) survival probability between the standard three-flavour model and a 3+1 model with $\Delta m_{41}^2 = 1 \text{ eV}^2$ and $\sin^2 \theta_{24} = 0.1$ for up-going neutrinos traveling through the Earth. Normal ordering is assumed and the standard oscillation parameter values are fixed to the NuFit 5.2 ones [4]. The other sterile parameters are set to 0. The L/E lines are shown in units of km/GeV. The oscillograms presented in this article are all computed with OscProb [19] using the Preliminary Reference Earth Model [20].

disappear in the 3+1 case at the first $\nu_\mu \rightarrow \nu_\tau$ standard oscillation maximum. The effect of the θ_{24} and θ_{34} mixing angles (assuming $\delta_{24} = 0$) on that feature is illustrated in the left panel of figure 2. As previously observed, when $\theta_{24} \neq 0$, the amplitude of the survival minimum is reduced. $\theta_{34} \neq 0$ has the same effect. The degeneracy between θ_{24} and θ_{34} can be partially lifted by the lower (average) ν_μ survival probability outside the minimum region seen in the case $\theta_{24} \neq 0$ but not for $\theta_{34} \neq 0$. In addition, this figure shows that when both active-sterile mixing angles are non-zero, the position of the minimum can be significantly shifted. This suggests that KM3NeT/ORCA could be particularly sensitive to simultaneously large values of θ_{24} and θ_{34} . The right panel of figure 2 illustrates that the δ_{24} phase also affects the position of the minimum, with a limited effect on its amplitude (compared to the mixing angles). The known degeneracy between the NMO and the sign of $\cos \delta_{24}$ [14] is also illustrated in figure 2 (right) as the curve obtained assuming IO and $\delta_{24} = 0$ overlaps the $\delta_{24} = \pi$ curve obtained in NO over most of the energy range considered. As all the effects mentioned here affect the $\nu_\mu \rightarrow \nu_\tau$ oscillations, degeneracies with the standard atmospheric parameters Δm_{31}^2 and θ_{23} are also expected. For instance, an apparent shift in Δm_{31}^2 could be accommodated by non-zero values for θ_{24} and θ_{34} .

3 The KM3NeT/ORCA detector

The KM3NeT collaboration is building two water Cherenkov neutrino telescopes at the bottom of the Mediterranean Sea [28]. The KM3NeT/ARCA (Astroparticle Research with Cosmics in the Abyss) detector, optimised for the detection of neutrinos from astrophysical sources in the TeV to PeV energy range, is located at a depth of about 3500 m, 80 km offshore Portopalo di Capo Passero in Sicily. The KM3NeT/ORCA (Oscillation Research

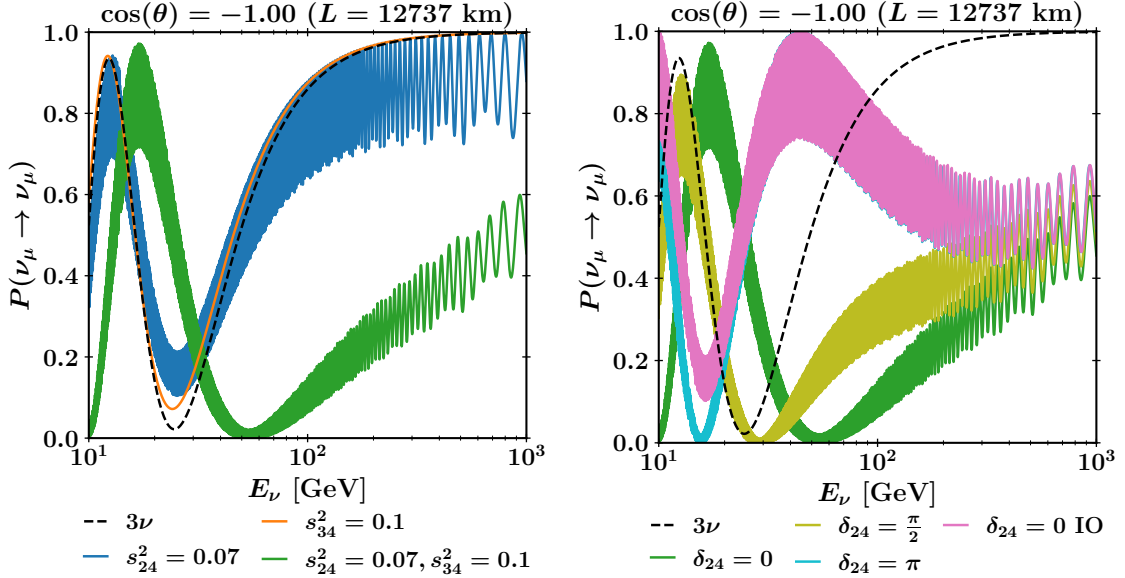


Figure 2. Muon neutrino survival probability as a function of E_ν , for vertically up-going neutrinos ($\cos \theta = -1.0$). Normal ordering is assumed except when mentioned otherwise, with NuFit 5.2 values [4] for the standard oscillation parameters. The three-flavour model (dashed black curve) is compared with various 3+1 models all assuming $\Delta m_{41}^2 = 1 \text{ eV}^2$. Left: different values of θ_{24} and θ_{34} ($s_{ij}^2 = \sin^2 \theta_{ij}$), with δ_{24} and other active-sterile mixing parameters fixed to 0. Right: different δ_{24} values, with $\sin^2 \theta_{24} = 0.07$, $\sin^2 \theta_{34} = 0.1$ and other active-sterile mixing parameters fixed to 0.

with Cosmics in the Abyss) detector, optimised for the determination of the NMO through the measurement of oscillations of GeV to TeV atmospheric neutrinos crossing the Earth, is located 40 km offshore Toulon (France) at a depth of about 2500 m. Oscillation studies in the KM3NeT/ORCA energy range are well-suited to probe Beyond the Standard Model (BSM) hypotheses such as the 3+1 sterile neutrino model.

Both detectors collect the Cherenkov light induced by the relativistic charged particles emerging from neutrino interactions. They consist of 3-dimensional arrays of glass spheres named Digital Optical Modules (DOMs) [29] housing 31 3-inch photomultiplier tubes (PMTs) each, arranged along flexible vertical structures called Detection Units (DUs) carrying 18 DOMs each. For KM3NeT/ORCA, the vertical spacing between DOMs is 9 m. Each DU is anchored to the seabed and remains vertical due to the buoyancy of the DOMs and of a buoy installed at its top. The DUs are arranged following a cylindrical footprint, with a horizontal spacing of 20 m. When completed, KM3NeT/ORCA will consist of 115 DUs, instrumenting a mass of sea water of around 7 Mton.

When the pulse resulting from the detection of a Cherenkov photon by a PMT reaches a certain threshold, a *hit* is generated. To save bandwidth, rather than digitizing the whole pulse, only the Time Over Threshold (ToT) of the pulse is recorded, along with the time of the hit and the PMT identifier. The hit information is sent to the onshore data processing

center for online data filtering. More information about the data acquisition system of KM3NeT can be found in [30]. *Events* are generated by trigger algorithms looking for causally-related hits on multiple DOMs. The trigger algorithms are designed to suppress background hits coming from dark counts (spontaneous electron emission from the photocathode of the PMTs) [31], bioluminescence [32–34], and natural radioactivity of ^{40}K present in the sea water [35]. The KM3NeT detectors are not sensitive to the detailed particle content of an event. Events are grouped into two topologies in KM3NeT/ORCA: *track-like* and *shower-like* events. Track-like events are caused by muons crossing the detector, encompassing ν_μ -CC interactions and ν_τ -CC interactions quickly followed by the decay of the τ lepton into a muon (branching ratio $\simeq 17.4\%$ [7]). Track-like events also include large amounts of down-going high-energy atmospheric muons which still reach the detectors despite the natural shielding provided by the sea water [36]. GeV muons travel in a straight line and lose energy continuously at a minimum rate of about 0.2 GeV/m. Hence, the induced hits are observed on DOMs distributed evenly inside a cylinder, whose axis is the muon trajectory. The other neutrino interaction channels (ν_e -CC, other ν_τ -CC, ν -NC) create particle cascades (hadronic and/or electromagnetic), and are hence shower-like events. They appear as a localised burst of light in the detector, with hits distributed inside an ellipsoid whose longitudinal extent is 10 m at most [28]. Based on the expected hit distributions, three trigger algorithms are applied in parallel: one looking for track-like events as sets of causally related hits within the volume of a cylinder, and two looking for shower-like events as sets of causally related hits within the volume of a sphere, with one of the two optimised for low-energy events.

Events are reconstructed assuming either a track or a shower model. More information about the track and shower reconstruction is given in refs. [37] and [38] respectively. Both procedures are iterative and use a maximum likelihood estimation based on the multi-dimensional probability density function of the photon arrival time on the PMTs.

To fulfill the physics goals of KM3NeT, good angular and energy resolutions must be achieved. Both require an accurate calibration of the detector. The KM3NeT detectors are huge infrastructures deployed in a changing environment which affects their performance over time. The position and orientation of the DOMs are measured every 10 minutes with an accuracy of 20 cm using an acoustic positioning system and sets of accelerometers and magnetometers located inside each DOM [39]. The synchronisation of all PMTs with an onshore master clock is ensured through a custom implementation of the White Rabbit protocol [40, 41]. As delays can occur at multiple levels of the infrastructure, the time calibration must be achieved at various scales: between the PMTs of a given DOM (intra-DOM), between the DOMs of a given DU (inter-DOM), and between the DUs (inter-DU). The intra-DOM calibration uses coincident hits induced by ^{40}K decays [42]; the inter-DOM calibration uses dedicated LED flashers called nanobeacons [43]; and the inter-DU calibration relies on the maximization of the quality of the reconstructed tracks of atmospheric muons [15, 44].

4 ORCA6 data sample and event selection

Data were taken with the ORCA6 configuration from January 2020 to November 2021, with a total detector livetime of 633 days. After applying the data quality cuts presented in [45], a total of 510 days of data taking remains, corresponding to a total exposure of 433 kton-years. This data sample was also used for other recently published ORCA6 oscillation analyses, comprising a standard neutrino oscillation analysis [45], a study of tau neutrinos and unitarity [46], searches for non-standard neutrino interactions [47], invisible neutrino decay [48] and quantum decoherence [49].

In order to remove accidental triggers, pre-selection cuts on the number of hits and the reconstructed track likelihood of the events are applied [45]. In addition, only events reconstructed as up-going are kept. Even though only a small fraction of atmospheric muons are misreconstructed as up-going, they constitute close to 99.9% of the accepted events at this stage, as the rate of reconstructed atmospheric muon events (≈ 7 Hz) exceeds that of neutrino events by 5 orders of magnitude.

The event selection and classification is performed using two dedicated sets of Boosted Decision Trees (BDTs), trained using Monte Carlo (MC) simulations (see section 5.1). Both BDTs are trained on (and applied to) events passing the pre-selection cuts only. The BDT models are built using variables related to the space and time distribution of the hits, as well as variables computed through the track and shower reconstruction chains, which are both applied to all triggered events. Each BDT model summarises the input features into a single output score. Details on the training and performances of the BDTs are given in [45]. The first BDT is used to separate neutrino events from the misreconstructed atmospheric muons events. It is able to identify poorly reconstructed atmospheric muons because they trigger more hits in the upper hemisphere of the DOMs and in the upper part of the DUs. Events with a high atmospheric muon BDT score are removed, resulting in a neutrino sample that contains 5828 events, with an expected muon contamination of a few percent. The goal of the second BDT is the separation between track-like and shower-like neutrino events. The resulting track sample is further divided in two classes: a *high purity* track class with an expected atmospheric muon contamination around 0.1%, and around 95% ν_μ -CC events; and a *low purity* track class with a few percent muon contamination and around 90% ν_μ -CC events. This selection leads to a total of 1868, 2002 and 1958 events in the high purity track, low purity track and shower classes respectively.

The track/shower separation gives some sensitivity to the flavour of the interacting neutrino, as events classified as tracks are mostly ν_μ -CC. However, around 45% of the selected shower-like events are low-energy (< 10 GeV) ν_μ -CC events, as short muon tracks cannot be easily distinguished from shower-like events. The low/high purity separation for track-like events increases the sensitivity to the standard oscillation parameters by isolating tracks with the best angular resolution in the high purity class [45]. For the eV-scale sterile neutrino search presented here, the same class definitions are kept, as the main

feature giving sensitivity to the active-sterile mixing angles of interest is the first $\nu_\mu \rightarrow \nu_\tau$ oscillation maximum (see section 2), the same used to measure θ_{23} and Δm_{31}^2 [45]. The reconstructed energy range for the two track classes is 2 GeV to 100 GeV. It is extended to 1 TeV for the shower class.

5 Analysis method

This analysis relies on comparing the observed numbers of reconstructed and selected events to the expected numbers, given a set of oscillation parameters of interest and nuisance parameters. This comparison is performed as a function of the reconstructed neutrino energy E and the cosine of the zenith angle $\cos\theta$.

5.1 Event distribution modeling and Monte Carlo simulations

To compute the expected number of events, the atmospheric neutrino flux is multiplied by the oscillation probabilities and weighted by the CC and NC interaction cross-sections, before accounting for the detector response. For the atmospheric neutrino flux, the year-averaged, solar minimum HKKM 2014 [50] flux tables computed for the Fréjus experiment site (located in Modane, 250 km away from the KM3NeT/ORCA site) are used. The OscProb software [19] is used to compute the oscillation probabilities, and the Earth density is described using the Preliminary Reference Earth Model [20]. The detector response is modeled through response matrices computed from MC simulations, briefly described in the following (see [28] and [51] for more details). The generation of neutrino events is performed using the GENIE-based [52] software gSeaGen [53]. Atmospheric muons are generated using the parametric generator MUPAGE [54]. The propagation of the Cherenkov photons induced along the path of the produced charged particles is performed using the Geant4-based [55] package KM3Sim [56]. For high-energy particles, a faster, custom KM3NeT package relying on probability density functions of the light arrival time is used instead of KM3Sim because of the large amounts of photons generated. The PMT response is simulated using another custom KM3NeT package which also includes the simulation of dark count and optical background, based on the trigger rates observed in the data for each PMT. From this point on, the output of the MC simulation chain is processed using the same trigger and event reconstruction algorithms (see section 3) and the same selection and classification procedure (see section 4) as for data. A 4-dimensional response matrix is built for each event class and each neutrino interaction channel, mapping the true neutrino energy and cosine of the zenith angle to the reconstructed ones. The choice of the binning used to build the response matrices is described in [45]. The full chain to compute response matrices and expected event distributions is implemented through the custom KM3NeT software *Swim* [57, 58].

5.2 Nuisance parameters

To model sources of systematic uncertainties, a total of 16 nuisance parameters are used in this analysis. Most are common to the standard oscillation analysis [45]:

- Uncertainties on the atmospheric neutrino flux shape and neutrino species ratios are modeled through corrections applied directly to the HKKM flux: on the ratio of up-going to horizontal neutrino (δ_θ), on the spectral index (δ_σ), and on the ratios of, respectively, ν_μ to $\bar{\nu}_\mu$ ($s_{\mu\bar{\mu}}$), ν_e to $\bar{\nu}_e$ ($s_{e\bar{e}}$), and $\nu_e + \bar{\nu}_e$ to $\nu_\mu + \bar{\nu}_\mu$ ($s_{e\mu}$).
- Uncertainties on neutrino cross-sections and on the selection and classification efficiencies are modeled through scaling factors affecting the normalisation of specific channels. The overall normalisation f_{all} scales all selected events. The normalisation of the NC (τ -CC) events f_{NC} ($f_{\tau\text{CC}}$) accounts for the uncertainty in modelling the NC interaction (τ -CC) cross-section and event selection. The f_{HPT} and f_{S} normalisations are used for the relative normalisation of the high purity track and shower classes. A normalisation for the atmospheric muon background f_μ is also used. An additional scaling factor f_{HE} is used to scale high-energy events to account for the different assumptions made on light propagation by the two different light propagation software packages mentioned in section 5.1. This scaling is applied for NC events with true energy above 100 GeV and for CC events with true energy above 500 GeV.
- Uncertainties on the water absorption and scattering lengths and the absolute PMT efficiency are accounted for through an energy scale parameter E_s . This parameter is applied as a shift in the true energy of the detector response. For more details and discussion about the implementation, see [59].

For the sterile neutrino search, Δm_{31}^2 and θ_{23} are also nuisance parameters. No prior uncertainty is assumed for θ_{23} . Δm_{31}^2 is constrained using the values and uncertainties reported by the Daya Bay collaboration [60]. The Daya Bay measurement, obtained from ν_e disappearance, can be considered uncorrelated with the sterile neutrino search presented in this work, which relies mostly on the ν_μ disappearance channel in a “no ν_e ” approximation (see section 6). The other standard oscillation parameters, for which KM3NeT/ORCA has no sensitivity, are fixed to the NuFit 5.0 values with Super-Kamiokande data included in the global fit [4] given in table 1. Finally, the δ_{24} phase which, as shown in figure 2, influences the position of the $\nu_\mu \rightarrow \nu_\tau$ standard oscillation maximum, is fitted without prior constraint.

Parameter	NO	IO
θ_{12}	33.44°	33.44°
θ_{13}	8.57°	8.60°
Δm_{21}^2 [10 ⁻⁵ eV ²]	7.42	7.42
δ_{CP}	197°	282°

Table 1. Values used for the non-fitted standard neutrino oscillation parameters, from NuFit 5.0 including Super-Kamiokande data [4].

5.3 Statistical methods

In the following, given an observed number of events n_{ij} of the class i in bin j , the parameters of interest of the model \vec{x} are determined through the minimisation of the following

negative log-likelihood function:

$$\begin{aligned}
-2 \ln \mathcal{L}(\vec{x}, \vec{\eta}) = & 2 \sum_{i=1}^{N_{\text{classes}}} \sum_{j=1}^{N_{\text{bins}}} \left[\beta_{ij} \mu_{ij}(\vec{x}, \vec{\eta}) - n_{ij} + n_{ij} \ln \left(\frac{n_{ij}}{\beta_{ij} \mu_{ij}(\vec{x}, \vec{\eta})} \right) + \frac{(\beta_{ij} - 1)^2}{\sigma_{\beta_{ij}}^2} \right] \\
& + \sum_{k=1} \left(\frac{\eta_k - \langle \eta_k \rangle}{\sigma_k} \right)^2,
\end{aligned} \tag{5.1}$$

where $\mu_{ij}(\vec{x}, \vec{\eta})$ is the expected event distribution for the set of parameters of interest \vec{x} and nuisance parameters $\vec{\eta}$. The β_{ij} factors act as additional nuisance parameters and are introduced to account for the finite number of generated MC events used to build the response matrices, following the Barlow and Beeston light method [61, 62] (see ref [58] for details). The term in square brackets corresponds to a Poissonian likelihood. The term in parentheses is a Gaussian penalisation term accounting for the prior uncertainties on the subset of constrained nuisance parameters: for a parameter η_k , $\langle \eta_k \rangle$ is the prior mean and σ_k is its standard deviation. In *Swim*, the parameters of interest \vec{x} and the nuisance parameters $\vec{\eta}$ are determined by minimising equation 5.1 using the MIGRAD solver of the Minuit2 package [63].

The test statistic used to build the confidence interval of the parameters of interest around their best-fit values is the logarithm of the likelihood ratio between each point of the phase-space of interest \vec{x} and the best-fit point $\vec{\hat{x}}$, written $-2\Delta \ln \mathcal{L}$ in the following. The confidence intervals of the parameters of interest are built in a frequentist way. Using Wilks' theorem [64], and not a full Feldman-Cousins confidence interval derivation [65] due to computing constraints, the allowed region of the parameter space given a certain confidence level is obtained by comparing the value of $-2\Delta \ln \mathcal{L}$ with the corresponding quantile of a χ^2 distribution with two degrees of freedom, as two is the dimension of the parameter space of interest.

5.4 Fitting procedure

For each point of the phase space of interest, equation 5.1 is minimised using two starting points for four nuisance parameters, to avoid getting stuck in local minima: normal and inverted ordering ($\Delta m_{31}^2 = \{2.541 \times 10^{-3}, -2.496 \times 10^{-3}\} \text{ eV}^2$); θ_{23} lower and upper octant ($\theta_{23} = \{40^\circ, 50^\circ\}$); energy scale E_s below and above 1.0 ($E_s = \{0.95, 1.05\}$); and δ_{24} below and above 180° ($\delta_{24} = \{90^\circ, 270^\circ\}$). This produces a total of 16 distinct starting points. The two start values for Δm_{31}^2 , θ_{23} and E_s are common to the standard oscillation analysis of ORCA6 [45]. For δ_{24} , the use of two start values is motivated by the observation of local minima when computing the $-2\Delta \ln \mathcal{L}$ profile of that parameter. In each fit, the parameter space is restricted to the NMO, θ_{23} octant and $(E_s - 1)$ sign corresponding to the start value. No limit is put on δ_{24} .

6 Results

The ORCA6 data sample is analysed under the $\Delta m_{41}^2 = 1 \text{ eV}^2$ hypothesis; the results hold for $\Delta m_{41}^2 > 1 \text{ eV}^2$ for which faster oscillations are unobservable. Simultaneous constraints on the mixing of the ν_μ and ν_τ states with the sterile state are obtained by scanning the $(|U_{\mu 4}|^2, |U_{\tau 4}|^2)$ space, with $U_{e 4} = 0$ (i.e. $\theta_{14} = \delta_{14} = 0$). In that case, the magnitude of the $U_{\mu 4}$ and $U_{\tau 4}$ mixing elements is expressed as:

$$|U_{\mu 4}|^2 = \sin^2 \theta_{24} \quad (6.1)$$

$$|U_{\tau 4}|^2 = \cos^2 \theta_{24} \sin^2 \theta_{34}. \quad (6.2)$$

For each fit δ_{24} is set free. To obtain the allowed region for the parameters of interest at a given confidence level, a 2-dimensional scan is performed by sampling the $(|U_{\mu 4}|^2, |U_{\tau 4}|^2)$ phase space uniformly in log scale, using 27 points between 1×10^{-3} and 0.5 (excluded) for both $|U_{\mu 4}|^2$ and $|U_{\tau 4}|^2$, with an additional point at 0.

6.1 Best-fit point

The position of the best-fit point \vec{x} is computed independently of the grid scan: fits with free $U_{\mu 4}$ and $U_{\tau 4}$ (thus free θ_{24} and θ_{34}) are performed. To avoid falling in potential local minima in the $(|U_{\mu 4}|^2, |U_{\tau 4}|^2)$ space, three pairs of starting values are used (in addition to the 16 sets of starting values already introduced): (0.0, 0.0), (0.5, 0.0) and (0.0, 0.5). This makes a total of 48 fits to determine the best-fit point, found at:

$$\begin{aligned} |U_{\mu 4}|^2 &= 6.89 \times 10^{-2} \\ |U_{\tau 4}|^2 &= 2.35 \times 10^{-4}, \end{aligned} \quad (6.3)$$

which in terms of mixing angles corresponds to $\theta_{24} = 15.2^\circ$ and $\theta_{34} = 0.9^\circ$. The values of the nuisance parameters obtained at the best-fit point are compared with their assumed prior uncertainty in table 2. The most significant deviations with respect to the results of the standard oscillations best fit, reported in table 4 of [45], are for the overall normalisation f_{all} , with $1.27_{-0.14}^{+0.15}$ in the sterile fit versus $1.11_{-0.13}^{+0.14}$ in the three-flavour fit, and the energy scale E_s with $1.10_{-0.07}^{+0.07}$ versus $1.03_{-0.08}^{+0.11}$. The higher overall normalisation in the sterile case is expected, as the average effect of the sterile neutrino is to decrease the number of neutrinos of other flavours. The difference in energy scale can be explained by the prior on Δm_{31}^2 used for the current sterile analysis but not for the standard oscillation analysis. Indeed, this prior strongly restricts the fit to values of $|\Delta m_{31}|^2$ close to $2.5 \times 10^{-3} \text{ eV}^2$ in the sterile analysis, while a value of $2.18 \times 10^{-3} \text{ eV}^2$ is found to match the data better in the standard oscillation analysis, where no external constraint on that parameter is imposed. Thus, in the sterile fit, the larger $|\Delta m_{31}|^2$ value imposed means that the L/E ratio should be scaled down to equivalently describe the event distributions. This means the fit favours a higher scaling of the energy, explaining the higher E_s seen in the sterile fit. The needed shift in energy induced by the larger $|\Delta m_{31}|^2$ value imposed in this analysis is also partially accommodated by the values of the sterile parameters (see section 2). For vertical up-going neutrinos, the position of the first $\nu_\mu \rightarrow \nu_\tau$ maximum is shifted by 2.4% (from 24.7 to 25.3

GeV) when comparing the oscillation probabilities of the 3+1 model at the best-fit point with the ones of the standard three-flavour model.

Parameter	Nominal value \pm uncertainty	Best Fit	Post-fit uncertainty
δ_θ	0.00 ± 0.02	-0.00	-0.02/+0.02
δ_γ	0.00 ± 0.30	-0.00	-0.03/+0.03
$s_{e\bar{e}}$	0.00 ± 0.07	0.01	-0.07/+0.07
$s_{\mu\bar{\mu}}$	0.00 ± 0.05	0.00	-0.05/+0.05
$s_{e\mu}$	0.00 ± 0.02	-0.00	-0.02/+0.02
$f_{\tau\text{CC}}$	1.00 ± 0.20	0.90	-0.18/+0.18
f_{NC}	1.00 ± 0.20	0.85	-0.19/+0.19
E_s	1.00 ± 0.09	1.10	-0.07/+0.07
f_{HE}	1.00 ± 0.50	1.57	-0.29/+0.32
f_{HPT}	1.00	0.92	-0.04/+0.04
f_S	1.00	0.89	-0.06/+0.06
f_μ	1.00	0.40	-0.31/+0.36
f_{all}	1.00	1.27	-0.14/+0.15
Δm_{31}^2 [10 ⁻³ eV ²]	2.541 ± 0.060	2.521	-0.059/+0.059
θ_{23} [°]	49.2	44.1	-4.1/+6.4
δ_{24} [°]	0	322	-322/+38

Table 2. Best-fit values and post-fit uncertainties at 68% CL of the nuisance parameters from the fit of ORCA6 data to $U_{\mu 4}$ and $U_{\tau 4}$ with $\Delta m_{41}^2 = 1$ eV². The fit is done in both mass orderings, and the best fit is found in NO.

6.2 ($|U_{\mu 4}|^2, |U_{\tau 4}|^2$) scan results

The log-likelihood ratio map resulting from the 2-dimensional grid scan, as well as upper limits of the allowed parameter space at confidence levels (CL) of 90%, 95% and 99%, are shown in figure 3 (left). A linear scale is used for the y axis so that the best fit, which is outside the scanned range, is visible. The (0, 0) point, with a value $-2\Delta \ln \mathcal{L}(0, 0) = 1.76$, is within the allowed region for the three CLs considered. This means that the ORCA6 data is fully compatible with the standard model. When profiling over the other mixing element, the upper limits at a 90% CL are found to be:

$$\begin{aligned} |U_{\mu 4}|^2 &< 0.138 \\ |U_{\tau 4}|^2 &< 0.076. \end{aligned} \tag{6.4}$$

In figure 3 (right), the 90% CL upper limits in $|U_{\mu 4}|^2$ and $|U_{\tau 4}|^2$ obtained by fitting the ORCA6 433 kton-years data set are compared with the ones obtained by fitting an Asimov MC data set generated using the data best-fit point values for the parameters of interest and the nuisance parameters (reported in table 2). This comparison shows that a larger region of the phase space is excluded when fitting the data, compared to the one expected from the Asimov sensitivity study. The stricter upper limits obtained when fitting the data can be understood by looking at the one-dimensional reconstructed L/E

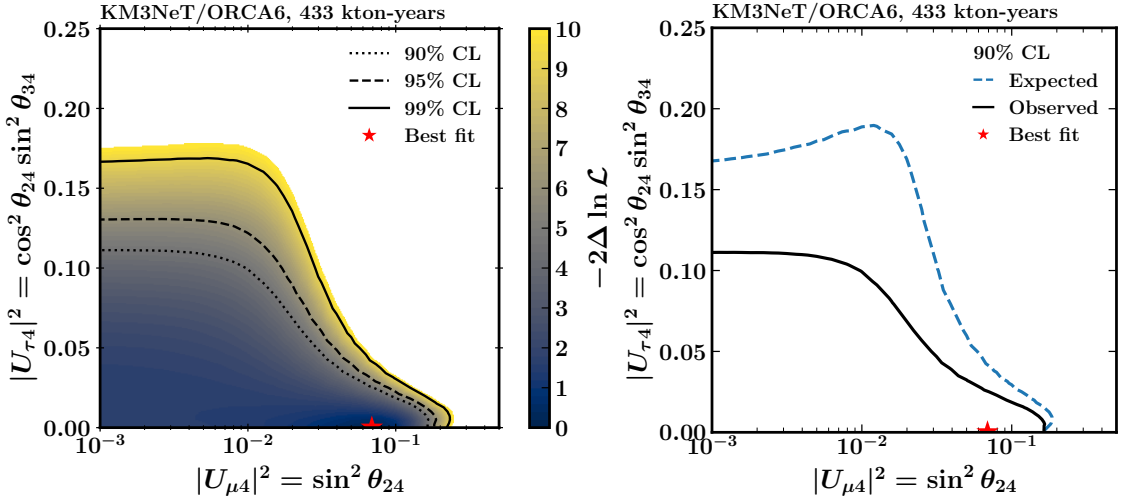


Figure 3. **Left:** Log-likelihood ratio map obtained from the ORCA6 data sample over the $|U_{\mu 4}|^2$ and $|U_{\tau 4}|^2$ phase space. $-2\Delta \log \mathcal{L}$ is not displayed when higher than 10 units. The black lines show upper limits of the allowed parameter space at various confidence levels. **Right:** Comparison of the observed and expected upper limits at 90% CL on the $U_{\mu 4}$ and $U_{\tau 4}$ mixing elements for ORCA6. The excluded regions are on the top right side of the contours.

event distributions of figure 4, shown for the three event classes. Both the data events and model best-fit point for this analysis are shown. The standard oscillation best fit is also shown for reference. It is barely distinguishable from the sterile best fit. The standard oscillation pattern is clearly visible in the high purity (and to a lower extent, low purity) track class. However, it is hardly distinguishable in the shower class, due to the mixture of flavours in this class. On the high purity tracks distribution, the data underfluctuates with respect to the model at the oscillation dip (corresponding to the first $\nu_{\mu} \rightarrow \nu_{\tau}$ maximum) at $L/E \sim \mathcal{O}(10^3)$ km/GeV. This is a crucial feature of the event distribution studied here as it constrains the model to give the deepest dip possible, which strongly favours maximal mixing for θ_{23} (as already reported in [45]). It also puts strong constraints on the active-sterile mixing angles θ_{24} and θ_{34} , with particularly strict limits on θ_{34} . Indeed, the effect of θ_{34} on the $P(\nu_{\mu} \rightarrow \nu_{\mu})$ first maximum is very similar to the effect of a θ_{23} value far from maximal mixing, as illustrated in figure 5, while θ_{24} lowers the survival probability outside the oscillation dip region. This explains why high values of θ_{34} are strongly rejected. For illustration, an arbitrarily high value of $|U_{\tau 4}|^2$ is chosen to draw the dashed orange curve in figure 4, showing that higher θ_{34} makes the oscillation dip shallower, and therefore even further away from the data.

6.3 Comparison with existing measurements

The ORCA6 upper limits at 90% CL are compared with the results of other experiments in figure 6. Table 3 summarizes how each analysis treats the 3+1 and standard oscillation parameters relevant for this measurement. All consider eV-scale sterile neutrinos, but do not report exactly the same Δm_{41}^2 validity range. The IceCube result is obtained by

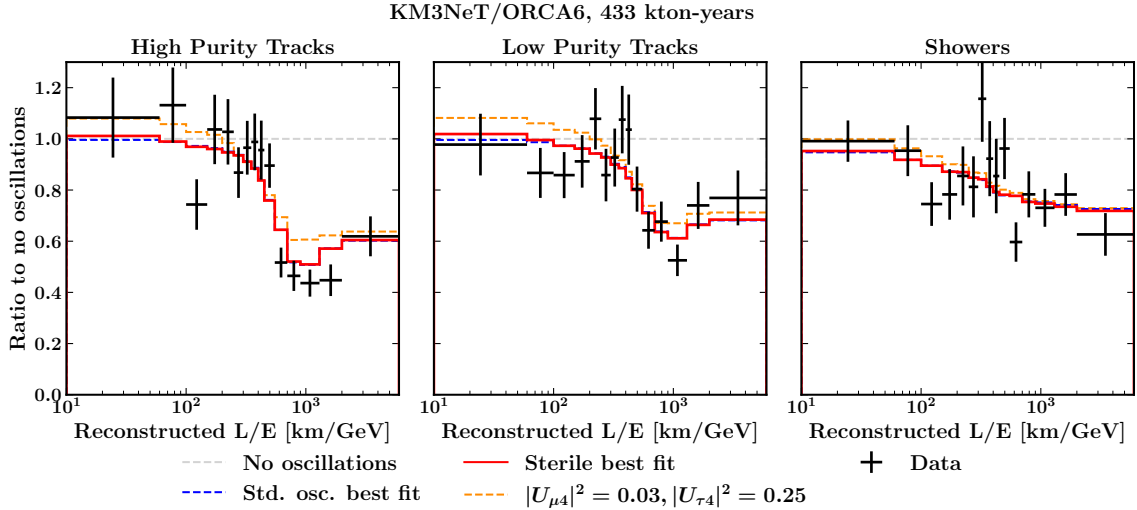


Figure 4. Event distributions in L/E for each class of the ORCA6 data (black), compared with the model prediction at the best-fit point in the eV sterile neutrino case (red) and in the standard oscillation case (dashed blue). The dashed orange curve shows the model prediction for an arbitrary point in the $(|U_{\mu 4}|^2, |U_{\tau 4}|^2)$ phase space.

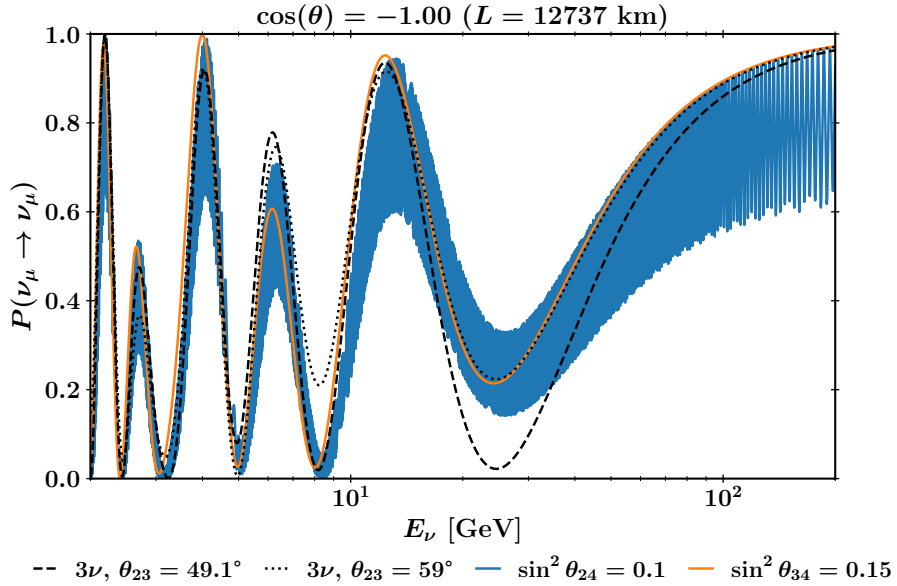


Figure 5. Muon neutrino survival probability as a function of the neutrino energy under various scenarios for $\cos \theta = -1.0$. The three-flavour standard oscillation model assuming the nominal value for $\theta_{23} = 49.1^\circ$ (dashed black) is compared with the three-flavour model with $\theta_{23} = 59^\circ$ (dotted black) and with the 3+1 models with $\sin^2 \theta_{24} = 0.1$ (blue) and $\sin^2 \theta_{34} = 0.15$ (orange), for $\Delta m_{41}^2 = 1 \text{ eV}^2$. All other sterile parameters are set to 0.

profiling over Δm_{41}^2 between 0.1 eV 2 and 50 eV 2 , with a best fit found at 5.0 eV 2 . All analyses considered here treat δ_{24} as a free nuisance parameter, with the exception of Super-Kamiokande and IceCube. The Super-Kamiokande analysis fixes $\delta_{24} = 0$, leading

to more restrictive limits than with a free δ_{24} . The IceCube analysis relies on the TeV disappearance feature which is less sensitive to δ_{24} . It uses $\delta_{24} = \pi$, as this choice was found to yield the most conservative limits. Regarding the mass ordering, only the ORCA6 and the ANTARES analyses consider both orderings. Finally, due to the partial degeneracies between θ_{23} and the θ_{24} and θ_{34} mixing angles (see figure 5), analyses lead with no constraint on this parameter (as done in this work, and for the DeepCore and ANTARES analysis) yield more conservative limits than the other analyses.

Experiment	Δm_{41}^2 range (eV ²)	δ_{24}	Mass ordering	Δm_{31}^2	θ_{23}
This work	≥ 1.0	Free	Both	Prior from [60]	Free
DeepCore [11]	≥ 1.0	Free	NO only	Free	
IceCube [10]	Profiled in [0.1, 50]	$= \pi$	Unknown	Unknown	
NOvA [66]	[0.05, 0.5]	Free	NO only	Fixed from [67]	
ANTARES [17]	≥ 0.5	Free	Both	Free	
SK [16]	≥ 0.1	$= 0$	NO only	Prior from [68]	

Table 3. Summary of the configurations used for the analyses compared in figure 6. The assumed Δm_{41}^2 validity range, and the treatment of δ_{24} , the mass ordering, Δm_{31}^2 and θ_{23} in the fits are reported. Other oscillation parameters do not have a significant impact on the $|U_{\mu 4}|^2$ and $|U_{\tau 4}|^2$ measurement.

The ORCA6 limits reported in figure 6 are competitive with the existing results, especially concerning the limit on the ν_τ mixing with the sterile state: only DeepCore, using 7.5 years of data, puts a stronger constraint on $|U_{\tau 4}|^2$. For $|U_{\mu 4}|^2$, ANTARES, IceCube, DeepCore and Super-Kamiokande all put stronger constraints than ORCA6, but these results were obtained with several years of data-taking from complete detectors, while the ORCA6 measurement was obtained with 1.4 years of data recorded with a detector that was 5% of its final size. The performance of KM3NeT/ORCA is due to its good sensitivity to ν_μ in the 20 – 30 GeV region which allows for the monitoring of the first $\nu_\mu \rightarrow \nu_\tau$ standard oscillation maximum. Other detectors have to rely on weaker effects at lower energy (e.g. Super-Kamiokande) or are optimised for slightly higher energies (e.g. ANTARES).

7 Conclusion

The first search for an eV-scale sterile neutrino performed with the KM3NeT/ORCA detector is presented in this article. In this analysis, a data sample collected with 6 detection units (5% of the complete detector size) is used, corresponding to an exposure of 433 kton-years and containing 5828 neutrino candidates. Constraints on the mixing of a hypothetical eV-scale sterile neutrino with the ν_μ and ν_τ states are established for $\Delta m_{41}^2 \geq 1$ eV². The results are compatible with the three-flavour standard model, and the upper limits obtained on $|U_{\mu 4}|^2$ and $|U_{\tau 4}|^2$ are compatible with the results reported by other experiments.

This result, although based on a limited detector size and statistics, highlights the significant potential of KM3NeT/ORCA. More specifically for eV-scale sterile neutrino

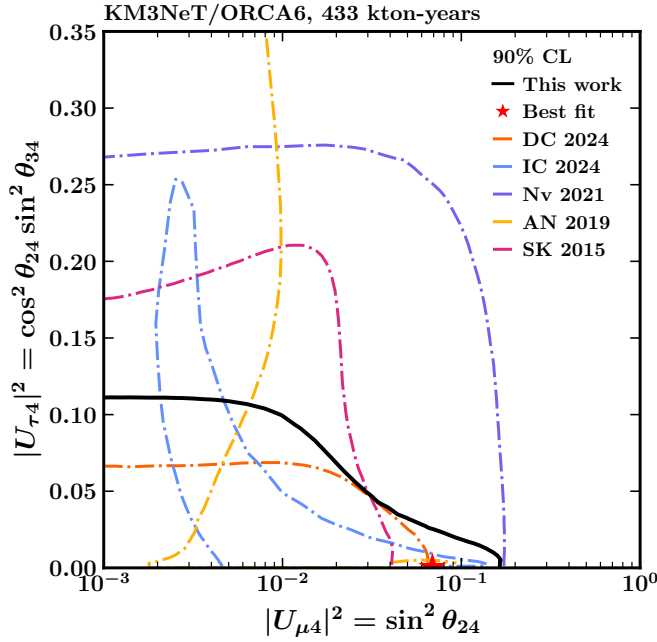


Figure 6. Comparison of the upper limits at 90% CL on $|U_{\mu 4}|^2$ and $|U_{\tau 4}|^2$ obtained by ORCA6 with previous measurements from Super-Kamiokande (SK) [16], NOvA (Nv) [66], ANTARES (AN) [17], IceCube (IC) [10] and DeepCore (DC) [11]. The excluded regions are on the top right side of the contours.

searches, it should be possible to probe the sterile-induced TeV resonance on $\bar{\nu}_\mu$ disappearance with the final configuration of KM3NeT/ORCA.

Acknowledgments

The authors acknowledge the financial support of: KM3NeT-INFRADEV2 project, funded by the European Union Horizon Europe Research and Innovation Programme under grant agreement No 101079679; Funds for Scientific Research (FRS-FNRS), Francqui foundation, BAEF foundation. Czech Science Foundation (GAČR 24-12702S); Agence Nationale de la Recherche (contract ANR-15-CE31-0020), Centre National de la Recherche Scientifique (CNRS), Commission Européenne (FEDER fund and Marie Curie Program), LabEx UnivEarthS (ANR-10-LABX-0023 and ANR-18-IDEX-0001), Paris Île-de-France Region, Normandy Region (Alpha, Blue-waves and Neptune), France, The Provence-Alpes-Côte d’Azur Delegation for Research and Innovation (DRARI), the Provence-Alpes-Côte d’Azur region, the Bouches-du-Rhône Departmental Council, the Metropolis of Aix-Marseille Provence and the City of Marseille through the CPER 2021-2027 NEUMED project, The CNRS Institut National de Physique Nucléaire et de Physique des Particules (IN2P3); Shota Rustaveli National Science Foundation of Georgia (SRNSFG, FR-22-13708), Georgia; This research was funded by the European Union (ERC MuSES project No 101142396); The General Secretariat of Research and Innovation (GSRI), Greece; Istituto Nazionale di Fisica Nucleare (INFN) and Ministero dell’Università e della Ricerca (MUR), through PRIN 2022 program (Grant PANTHEON 2022E2J4RK, Next Generation EU) and PON R&I program (Avviso n. 424 del 28 febbraio 2018, Progetto PACK-PIR01 00021), Italy; IDMAR project Po-Fesr Sicilian Region az. 1.5.1; A. De Benedictis, W. Idrissi Ibnsalih, M. Bendahman, A. Nayerhoda, G. Papalashvili, I. C. Rea, A. Simonelli have been supported by the Italian Ministero dell’Università e della Ricerca (MUR), Progetto CIR01 00021 (Avviso n. 2595 del 24 dicembre 2019); KM3NeT4RR MUR Project National Recovery and Resilience Plan (NRRP), Mission 4 Component 2 Investment 3.1, Funded by the European Union – NextGenerationEU, CUP I57G21000040001, Concession Decree MUR No. n. Prot. 123 del 21/06/2022; Ministry of Higher Education, Scientific Research and Innovation, Morocco, and the Arab Fund for Economic and Social Development, Kuwait; Nederlandse organisatie voor Wetenschappelijk Onderzoek (NWO), the Netherlands; The grant ”AstroCeNT: Particle Astrophysics Science and Technology Centre”, carried out within the International Research Agendas programme of the Foundation for Polish Science financed by the European Union under the European Regional Development Fund; The program: ’Excellence initiative-research university’ for the AGH University in Krakow; The ARTIQ project: UMO-2021/01/2/ST6/00004 and ARTIQ/0004/2021; Ministry of Education and Scientific Research, Romania; Slovak Research and Development Agency under Contract No. APVV-22-0413; Ministry of Education, Research, Development and Youth of the Slovak Republic; MCIN for PID2021-124591NB-C41, -C42, -C43 and PDC2023-145913-I00 funded by MCIN/AEI/10.13039/501100011033 and by ”ERDF A way of making Europe”, for ASFAE/2022/014 and ASFAE/2022 /023 with funding from the EU NextGenerationEU (PRTR-C17.I01) and Generalitat Valenciana, for Grant AST22.6.2 with funding from Consejería de Universidad, Investigación e Innovación and Gobierno de España and European Union - NextGenerationEU, for CSIC-INFRA23013 and for CNS2023-144099, Generalitat Valenciana for CIDEGENT/2020/049, CIDEGENT/2021/23, CIDEIG/2023/20, ESGENT2024/24, CIPROM/2023/51, GRISOLIAP/2021/192 and INNVA1/2024/110 (IVACE+i), Spain; Khalifa University internal

grants (ESIG-2023-008, RIG-2023-070 and RIG-2024-047), United Arab Emirates; The European Union's Horizon 2020 Research and Innovation Programme (ChETEC-INFRA - Project no. 101008324).

Views and opinions expressed are those of the author(s) only and do not necessarily reflect those of the European Union or the European Research Council. Neither the European Union nor the granting authority can be held responsible for them.

References

- [1] SUPER-KAMIOKANDE collaboration, *Evidence for Oscillation of Atmospheric Neutrinos*, *Phys. Rev. Lett.* **81** (1998) 1562.
- [2] MACRO collaboration, *Measurement of the atmospheric neutrino-induced upgoing muon flux using MACRO*, *Physics Letters B* **434** (1998) 451.
- [3] P.B. Denton, M. Friend, M.D. Messier, H.A. Tanaka, S. Böser, J.A.B. Coelho et al., *Snowmass Neutrino Frontier: NF01 Topical Group Report on Three-Flavor Neutrino Oscillations*, arXiv:2212.00809 (2022), [DOI](#).
- [4] I. Esteban, M. Gonzalez-Garcia, M. Maltoni, T. Schwetz and A. Zhou, *The fate of hints: Updated global analysis of three-flavor neutrino oscillations*, *J. High Energ. Phys.* **2020** (2020) 178.
- [5] M.A. Acero, C.A. Argüelles, M. Hostert, D. Kalra, G. Karagiorgi, K.J. Kelly et al., *White Paper on Light Sterile Neutrino Searches and Related Phenomenology*, arXiv:2203.07323 (2023), [DOI](#).
- [6] J. Lesgourgues and S. Pastor, *Massive neutrinos and cosmology*, *Physics Reports* **429** (2006) 307.
- [7] PARTICLE DATA GROUP collaboration, *Review of Particle Physics*, *Phys. Rev. D* **110** (2024) 030001.
- [8] ALEPH, DELPHI, L3, OPAL, SLD collaborations, *Precision electroweak measurements on the Z resonance*, *Physics Reports* **427** (2006) 257.
- [9] ICECUBE collaboration, *Search for an eV-Scale Sterile Neutrino Using Improved High-Energy ν_μ Event Reconstruction in IceCube*, *Phys. Rev. Lett.* **133** (2024) 201804.
- [10] ICECUBE collaboration, *Exploration of mass splitting and muon/tau mixing parameters for an eV-scale sterile neutrino with IceCube*, *Physics Letters B* **858** (2024) 139077.
- [11] ICECUBE collaboration, *Search for a light sterile neutrino with 7.5 years of IceCube DeepCore data*, *Phys. Rev. D* **110** (2024) 072007.
- [12] L. Wolfenstein, *Neutrino oscillations in matter*, *Phys. Rev. D* **17** (1978) 2369.
- [13] C. Giunti and C.W. Kim, *Fundamentals of Neutrino Physics and Astrophysics*, Oxford University Press, UK, Oxford (2007), [10.1093/acprof:oso/9780198508717.001.0001](https://doi.org/10.1093/acprof:oso/9780198508717.001.0001).
- [14] KM3NET collaboration, *Sensitivity to light sterile neutrino mixing parameters with KM3NeT/ORCA*, *J. High Energ. Phys.* **2021** (2021) 180.
- [15] L. Bailly-Salins, *Atmospheric Muon Studies and Light Sterile Neutrino Search with KM3NeT/ORCA*, Ph.D. thesis, Normandie Université, 2024. <https://theses.hal.science/tel-04823223v1>.
- [16] SUPER-KAMIOKANDE collaboration, *Limits on sterile neutrino mixing using atmospheric neutrinos in Super-Kamiokande*, *Phys. Rev. D* **91** (2015) 052019.
- [17] ANTARES collaboration, *Measuring the atmospheric neutrino oscillation parameters and constraining the 3+1 neutrino model with ten years of ANTARES data*, *J. High Energ. Phys.* **2019** (2019) 113.
- [18] KM3NET collaboration, *Sensitivity of KM3NeT/ORCA6 to light sterile neutrino mixing parameters*, in *Neutrino 2024*, (Milano, Italy), Zenodo (2024), [DOI](#).

[19] J. Coelho, R. Pestes, A. Domi, S. Bourret, U. Rahaman, L. Maderer et al., *joaoabcoelho/oscprob: v2.0.12*, 2023. 10.5281/zenodo.10104847.

[20] A.M. Dziewonski and D.L. Anderson, *Preliminary reference Earth model*, *Physics of the Earth and Planetary Interiors* **25** (1981) 297.

[21] H. Nunokawa, O.L.G. Peres and R. Zukanovich Funchal, *Probing the LSND mass scale and four neutrino scenarios with a neutrino telescope*, *Physics Letters B* **562** (2003) 279.

[22] Ermilova, V. K., Tsarev, V. A. and Chechin, V. A., *Buildup of neutrino oscillations in the Earth*, *JETP Letters* **43** (1986) 353.

[23] S.P. Mikheyev and A.Y. Smirnov, *Resonant neutrino oscillations in matter*, *Progress in Particle and Nuclear Physics* **23** (1989) 41.

[24] S. Razzaque and A.Y. Smirnov, *Searching for sterile neutrinos in ice*, *J. High Energ. Phys.* **2011** (2011) 84.

[25] S. Razzaque and A.Y. Smirnov, *Searches for sterile neutrinos with IceCube DeepCore*, *Phys. Rev. D* **85** (2012) 093010.

[26] A. Esmaili, F. Halzen and O.L.G. Peres, *Constraining sterile neutrinos with AMANDA and IceCube atmospheric neutrino data*, *J. Cosmol. Astropart. Phys.* **2012** (2012) 041.

[27] ICECUBE collaboration, *Searching for eV-scale sterile neutrinos with eight years of atmospheric neutrinos at the IceCube neutrino telescope*, *Phys. Rev. D* **102** (2020) 052009.

[28] KM3NET collaboration, *Letter of intent for KM3NeT 2.0*, *J. Phys. G* **43** (2016) 084001.

[29] KM3NET collaboration, *The KM3NeT multi-PMT optical module*, *J. Inst.* **17** (2022) P07038.

[30] KM3NET collaboration, *The KM3NeT data acquisition system - Status and evolution*, *EPJ Web Conf.* **280** (2023) 08004.

[31] KM3NET collaboration, *Characterisation of the Hamamatsu photomultipliers for the KM3NeT Neutrino Telescope*, *J. Inst.* **13** (2018) P05035.

[32] S.H.D. Haddock, M.A. Moline and J.F. Case, *Bioluminescence in the sea*, *Ann Rev Mar Sci* **2** (2010) 443.

[33] E. Widder, *Bioluminescence and the Pelagic Visual Environment*, *Marine and Freshwater Behaviour and Physiology* **35** (2002) 1.

[34] J. Aguzzi, E. Fanelli, T. Ciuffardi, A. Schirone and J. Craig, *Inertial bioluminescence rhythms at the Capo Passero (KM3NeT-Italia) site, Central Mediterranean Sea*, *Sci Rep* **7** (2017) 44938.

[35] KM3NET collaboration, *Dependence of atmospheric muon flux on seawater depth measured with the first KM3NeT detection units*, *Eur. Phys. J. C* **80** (2020) 99.

[36] KM3NET collaboration, *Atmospheric muons measured with the KM3NeT detectors in comparison with updated numeric predictions*, *Eur. Phys. J. C* **84** (2024) 696.

[37] B. O Fearraigh, *Following the Light - Novel Event Reconstruction Techniques for Neutrino Oscillation Analyses in KM3NeT/ORCA*, Ph.D. thesis, Amsterdam University, 2024. <https://dare.uva.nl/search?identifier=c0d5bde5-b513-4291-a4df-fbf4d5c69add>.

[38] A. Domi, *Shower Reconstruction and Sterile Neutrino Analysis with KM3NeT/ORCA and Antares*, these de doctorat, Aix-Marseille, 2019. <https://theses.fr/2019AIXM0550>.

[39] KM3NET collaboration, *Dynamical position and orientation calibration of the KM3NeT telescope*, in *PoS(ICRC2023)*, vol. 444, p. 1033, SISSA Medialab, 2023, [DOI](#).

[40] J. Serrano, P. Alvarez, M. Cattin, E.G. Cota and P.M.J.H. Lewis, *The White Rabbit Project*, in *Proceedings of ICALEPICS TUC004*, (Kobe, Japan), 2009, <https://proceedings.jacow.org/icalepcs2009/papers/tuc004.pdf>.

[41] KM3NET collaboration, *KM3NeT broadcast optical data transport system*, *J. Inst.* **18** (2023) T02001.

[42] KM3NET collaboration, *In-Situ Calibration of KM3NeT*, in *Proceedings of 35th International Cosmic Ray Conference — PoS(ICRC2017)*, (Bexco, Busan, Korea), p. 1059, Sissa Medialab, 2017, [DOI](#).

[43] KM3NET collaboration, *Nanobeacon: A time calibration device for the KM3NeT neutrino telescope*, *Nuclear Instruments and Methods in Physics Research Section A: Accelerators, Spectrometers, Detectors and Associated Equipment* **1040** (2022) 167132.

[44] KM3NET collaboration, *Time, position and orientation calibration using atmospheric muons in KM3NeT*, in *PoS(ICRC2023)*, vol. 444, p. 218, SISSA Medialab, 2023, [DOI](#).

[45] KM3NET collaboration, *Measurement of neutrino oscillation parameters with the first six detection units of KM3NeT/ORCA*, *J. High Energ. Phys.* **2024** (2024) 206.

[46] S. Aiello, A. Albert, A.R. Alhebsi, M. Alshamsi, S. Alves Garre, A. Ambrosone et al., *Study of tau neutrinos and non-unitary neutrino mixing with the first six detection units of KM3NeT/ORCA*, *J. High Energ. Phys.* **2025** (2025) 213.

[47] KM3NET collaboration, *Search for non-standard neutrino interactions with the first six detection units of KM3NeT/ORCA*, *J. Cosmol. Astropart. Phys.* **2025** (2025) 073.

[48] KM3NET collaboration, *Probing invisible neutrino decay with the first six detection units of KM3NeT/ORCA*, *J. High Energ. Phys.* **2025** (2025) 105.

[49] KM3NET collaboration, *Search for quantum decoherence in neutrino oscillations with six detection units of KM3NeT/ORCA*, *J. Cosmol. Astropart. Phys.* **2025** (2025) 039.

[50] M. Honda, M.S. Athar, T. Kajita, K. Kasahara and S. Midorikawa, *Atmospheric neutrino flux calculation using the NRLMSISE-00 atmospheric model*, *Phys. Rev. D* **92** (2015) 023004.

[51] KM3NET collaboration, *Determining the neutrino mass ordering and oscillation parameters with KM3NeT/ORCA*, *Eur. Phys. J. C* **82** (2022) 26.

[52] C. Andreopoulos, A. Bell, D. Bhattacharya, F. Cavanna, J. Dobson, S. Dytman et al., *The GENIE neutrino Monte Carlo generator*, *Nuclear Instruments and Methods in Physics Research Section A: Accelerators, Spectrometers, Detectors and Associated Equipment* **614** (2010) 87.

[53] KM3NET collaboration, *gSeaGen: The KM3NeT GENIE-based code for neutrino telescopes*, *Computer Physics Communications* **256** (2020) 107477.

[54] G. Carminati, M. Bazzotti, A. Margiotta and M. Spurio, *Atmospheric MUons from PArametric formulas: A fast Generator for neutrino telescopes (MUPAGE)*, *Comp. Phys. Comm.* **179** (2008) 915.

[55] S. Agostinelli, J. Allison, K. Amako, J. Apostolakis, H. Araujo, P. Arce et al., *Geant4—a simulation toolkit*, *Nuclear Instruments and Methods in Physics Research Section A: Accelerators, Spectrometers, Detectors and Associated Equipment* **506** (2003) 250.

[56] A.G. Tsirigotis, A. Leisos and S.E. Tzamarias, *HOU Reconstruction & Simulation (HOURS): A complete simulation and reconstruction package for very large volume underwater neutrino telescopes*, *Nuclear Instruments and Methods in Physics Research Section A: Accelerators, Spectrometers, Detectors and Associated Equipment* **626–627** (2011) S185.

[57] S. Bourret, *Neutrino Oscillations and Earth Tomography with KM3NeT-ORCA*, Ph.D. thesis, Université Sorbonne Paris Cité, 2018. <https://theses.hal.science/tel-02491394v1>.

[58] V. Carretero Cuenca, *Neutrino Oscillations and Invisible Decay with the KM3NeT/ORCA Detector*, Ph.D. thesis, Universitat de Valencia, Valencia, 2024. <https://hdl.handle.net/10550/96472>.

[59] T.N. Chau, *Study of Atmospheric Neutrino Oscillations with the Deep-Sea Cherenkov Detector KM3NeT/ORCA and Synergies with Reactor Neutrinos*, Ph.D. thesis, Université Paris Cité, 2021. <https://theses.hal.science/tel-03999509>.

[60] DAYA BAY collaboration, *Precision Measurement of Reactor Antineutrino Oscillation at Kilometer-Scale Baselines by Daya Bay*, *Phys. Rev. Lett.* **130** (2023) 161802.

[61] R. Barlow and C. Beeston, *Fitting using finite Monte Carlo samples*, *Computer Physics Communications* **77** (1993) 219.

[62] J. Conway, *Incorporating Nuisance Parameters in Likelihoods for Multisource Spectra*, in the *proceedings of the PHYSTAT 2011*, pp. 115–120 (2011), DOI.

[63] “ROOT::Minuit2::MnMigrad Class Reference.” https://root.cern.ch/doc/master/classROOT_1_1Minuit2_1_1MnMigrad.html.

[64] S.S. Wilks, *The Large-Sample Distribution of the Likelihood Ratio for Testing Composite Hypotheses*, *The Annals of Mathematical Statistics* **9** (1938) 60.

[65] G.J. Feldman and R.D. Cousins, *Unified approach to the classical statistical analysis of small signals*, *Phys. Rev. D* **57** (1998) 3873.

[66] NOvA collaboration, *Search for Active-Sterile Antineutrino Mixing Using Neutral-Current Interactions with the NOvA Experiment*, *Phys. Rev. Lett.* **127** (2021) 201801.

[67] PARTICLE DATA GROUP collaboration, *Review of Particle Physics*, *Phys. Rev. D* **98** (2018) 030001.

[68] T2K collaboration, *Precise Measurement of the Neutrino Mixing Parameter θ_{23} from Muon Neutrino Disappearance in an Off-Axis Beam*, *Phys. Rev. Lett.* **112** (2014) 181801.